Solar Energy Materials and Solar Cells 172 (2017) 270–276

Contents lists available at ScienceDirect

Solar Energy Materials and Solar Cells

journal homepage: www.elsevier.com/locate/solmat

Solvent-assisted crystallization via a delayed-annealing approach for highly efficient hybrid mesoscopic/planar perovskite solar cells

Albertus Adrian Sutanto[a,b,c], Shiang Lan[d], Chih-Fu Cheng[a], Sandeep B. Mane[a], Hui-Ping Wu[d], Mario Leonardus[d,f], Meng-Yu Xie[a,e], Shih-Chieh Yeh[a], Chiao-Wei Tseng[a], Chin-Ti Chen[a], Eric Wei-Guang Diau[d,*], Chen-Hsiung Hung[a,*]

[a] Institute of Chemistry, Academia Sinica, Academia Road, Nankang, Taipei, Taiwan
[b] Department of Chemical Engineering, National Taiwan University of Science and Technology, Taipei 10607, Taiwan
[c] Department of Chemical Engineering, Faculty of Engineering, Diponegoro University, Semarang 50275, Indonesia
[d] Department of Applied Chemistry and Institute of Molecular Science, National Chiao Tung University, Hsinchu, Taiwan
[e] Department of Chemistry and Biochemistry, National Chung Cheng University, Chiayi 62102, Taiwan
[f] Sustainable Chemical Science and Technology-Taiwan International Graduate Program, Academia Sinica, Nankang, Taipei 11529 Taiwan

ARTICLE INFO

Keywords:
Perovskite solar cells
Hybrid mesoscopic
Solvent assisted crystallization
Delayed annealing
Perovskite morphology

ABSTRACT

The formation of a dense and uniform perovskite film with large grain is an important factor for getting excellent device performance. Here, we report an optimized solvent-assisted crystallization procedure followed by a delayed annealing for easy and reproducible fabrications of perovskite solar cells with a hybrid mesoscopic configuration. The working electrode contains a mesoporous TiO_2 scaffold layer of 100 nm deposited on FTO substrate with a thin TiO_2 blocking layer. The devices in this study were assembled using all commercially available materials without any extensive modification. Formation of uniform and pin-hole free perovskite nanocrystals with film thickness 200 nm on top of the scaffold layer was achieved via an optimized solvent-assisted crystallization method. A much smoother perovskite layer was achieved with a delayed annealing for a certain period. The best performing device was obtained at the annealing delayed for 60 min, giving the power conversion efficiency 16.9% with an average value 15.4% obtained from 60 devices.

1. Introduction

Solution processed thin-film solar cells such as dye-sensitized solar cells [1], quantum dot solar cells [2,3], organic solar cells [4,5] and heterojunction solar cells [6] are regarded as promising alternative for development of new generation photovoltaic devices. Perovskite solar cells (PSCs) based on hybrid organometallic halide nanocrystals as light absorbers have attracted substantial attention due to their remarkable photovoltaic performance and cost-effective processing. Additionally these perovskites possess excellent optical properties [7], ambipolar charge transport [8] and sufficient electron-hole diffusion lengths [9,10]. The power conversion efficiency (PCE) of the PSCs has been rocket-boosted from less than 10% to over 20% in just three years [2,11,12]. The highest reported PCE so far is 22.1% achieved by Seok and co-workers [13]. Two major device architectures, namely mesoscopic [14–19] and planar heterojunction [20,21], have been utilized to achieve the PCEs higher than 16%. Although the planar devices have achieved greater efficiencies, the effect of hysteresis was reported to be significant in solar cells of this type [22–27]. A high contact resistance for electron transfer between perovskite layer and dense TiO_2 layer in the planar heterojunction structure is proposed to be responsible for the hysteresis [26]. Considering of this, the addition of a mesoporous TiO_2 layer would offer a lower contact resistance for forward electron transfer from the perovskite due to its higher surface area, relieving the severity of hysteresis effect in mesoscopic nanocomposite device structure. Moreover, an optimally thick mesoporous TiO_2 layer will improve the efficient charge collection from perovskite layer via the large surface area of mesoporous TiO_2 layer [16]. The formation of a dense and uniform perovskite film with large crystal size is an important factor for getting excellent device performance. In addition, the grain size and grain boundary of perovskite play a crucial role on overall device performance. For example, several groups have reported the micro-scale kinetics of perovskite films using the imaging techniques of micro-photoluminescence, micro-electroluminescence and photoconductive atomic force microscopy [28–30]. Those results show that the device performance depends on the surface morphology of the

* Corresponding authors.
E-mail addresses: diau@mail.nctu.edu.tw (E.W.-G. Diau), chhung@gate.sinica.edu.tw (C.-H. Hung).

http://dx.doi.org/10.1016/j.solmat.2017.07.043
Received 24 November 2015; Received in revised form 1 July 2017; Accepted 30 July 2017

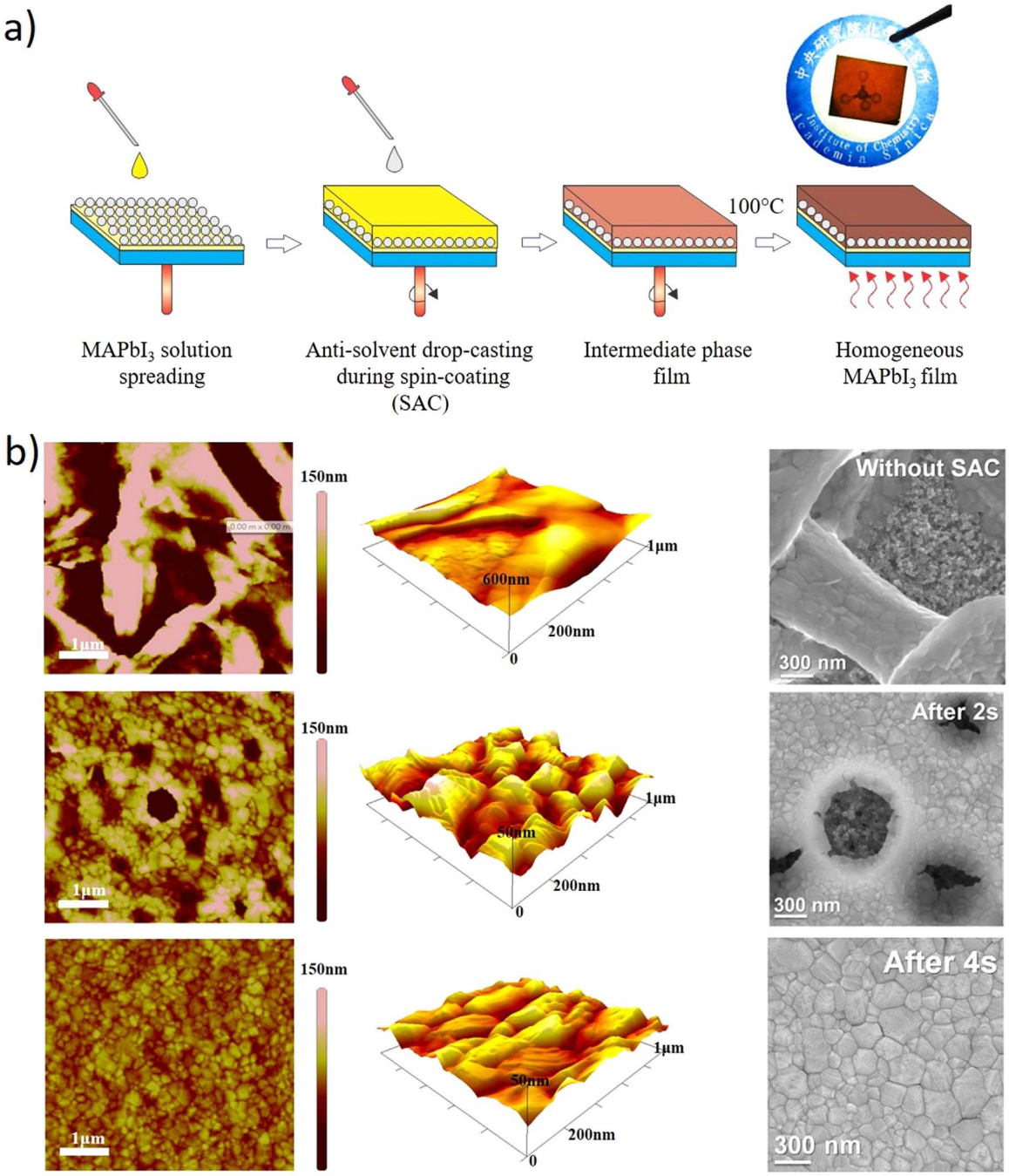

Fig. 1. a) Schematic illustration of solvent assisted crystallization method and b) AFM and SEM images of the $MAPbI_3$ surface prepared by adding chlorobenzene at different times after the start of spin-coating.

film; large grain size and less grain boundary in bulk perovskite significantly promote the efficiency of the cell.

The methylammonium lead iodide ($MAPbI_3$) perovskite layer can be prepared by several methods including one-step spin-coating method [31,32], two-step sequential deposition method [14,33] and vapour deposition method [34]. However, normal spin-coating method cannot form a homogeneous and uniform film with a large surface area. Use of an anti-solvent method during the spin coating process has been found to produce highly uniform and dense perovskite layer [16]. Jeon et al. have reported a bilayer perovskite architecture using poly(triarylamine) (PTAA) as a hole-transporting material (HTM) to obtain the highest efficiency of 16.5% and the average efficiency of approximately 15.2% calculated for over 100 devices [16]. They have utilized toluene as an anti-solvent in a two-step spin-coating method. A one-step, solvent-induced fast crystallization method also has been introduced for planar PSCs, through which highly flat and uniform $MAPbI_3$ thin films have been produced. By utilizing this faster and facile solution processing method, the optimized device showed a promising PCE 16.2% [35]. Although the reported device performance is promising, the low average efficiency and the hysteresis effect in those planar PSC devices could be a major obstacle for its widespread application.

In addition to modification of spin-coating conditions for increasing the grain size of the perovskite layer, some post-treatment methods also have been reported in order to improve the morphology of perovskite film. Post-annealing treatment using solvent vapour has been investigated by several groups [36–38]. Solvent post-annealing was first reported by Xiao et al. on p-type device configuration [36]. The solvent post-treatment was an effective method to increase the perovskite layer

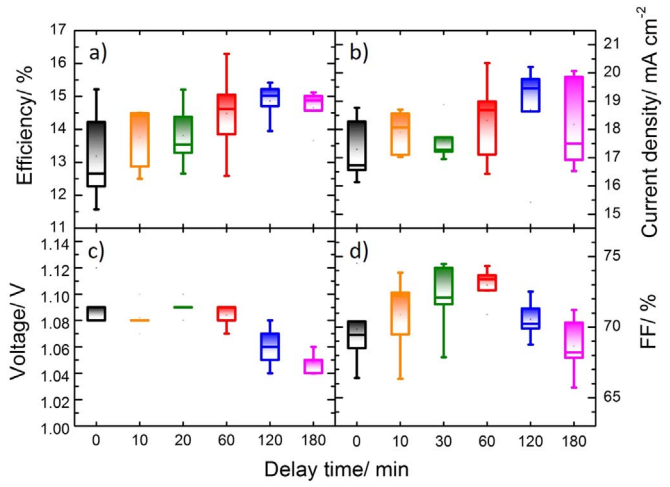

Fig. 2. Photovoltaic parameters represented as box plots for SAC-treated PSC devices as a function of annealing delayed period for a) power conversion efficiency (PCE/%), b) short-circuit current density (J_{SC}/mA cm^{-2}), c) open-circuit voltage (V_{OC}/V) and d) fill factor (FF). In the box plots, the outside whisker error bars represent the maximum and minimum of the data with ± 2.698 standard deviations (σ), and the two box edges represent the upper/lower quartiles of the data (± 0.6745σ) covering 50% of the data.

grain size and crystallinity [36]. Improvement in perovskite morphology is due to the condensation of solvent vapour on the surface and void area on the perovskite layer which resulting in elimination of grain boundaries and rearrangement of perovskite layer [37]. Crystallinity enhancement of the perovskite layer also could be achieved by a combined moisture pre-treatment followed by hot-air annealing method [39]. Post-annealing under ultra-dry gas flow has been reported that it could improve perovskite capping layer crystallinity and induce the formation of low defects perovskite crystal grain in mesoscopic device structure [40].

Along with the high PCE, high average efficiency, cost-effective process, and cheaper starting materials are also important factors to be considered for the commercialization of PSCs. Higher average efficiencies confirm the relative stability and reproducibility of the PSC devices [14,16,41]. The higher individual and average efficiencies have been obtained by compositional and structural manipulation of the perovskite material and/or by modifying the TiO_2 nanostructures. Herein we report a simple and economical procedure to obtain reproducible hybrid mesoscopic PSCs with average PCE of 15.4% (s.d. ± 0.74) assembled with all commercial materials by adopting the optimized one-step spin-coating procedure with solvent-assisted crystallization (SAC) followed by a delayed annealing for a certain period. The delay annealing has for the first time been applied in PSCs prepared by solvent-assisted crystallization method. Our results showed an enhancement in $MAPbI_3$ perovskite layer morphology which will provide an improved protocol for the preparation of hybrid mesoscopic PSCs by solvent-assisted crystallization method.

2. Experimental

2.1. Perovskite solar cell device fabrication

Fluorine doped Tin Oxide (FTO) glass (TEC-15, solaronix) was patterned by chemical etching with Zn powder and 2 M HCl solution. The etched substrate was then cleaned with Extran® MA 02 (MERCK) and ultrasonically cleaned with deionized water, acetone, and 2-propanol in sequence for 10 min, respectively. After drying under N_2 stream, the substrates were further cleaned by O_2 plasma cleaner. A dense layer of TiO_2 was then coated on the substrates by spray pyrolysis of titanium diisopropoxide bis(acetylacetone) (75 wt% in isopropanol, Aldrich) diluted in absolute ethanol (v/v, 1/20) at 500 °C. A mesoporous layer of TiO_2 was then deposited by spin-coating TiO_2 paste (Dyesol 18NR-T) diluted in absolute ethanol at 1:12 weight ratio at 5000 rpm for 30 s. The substrates were then heated at 180 °C for 5 min, followed by annealing at 550 °C for 30 min. The perovskite and HTM layer deposition was carried out in a nitrogen-filled glovebox. The perovskite precursor solution was freshly prepared before use by treating methylammonium iodide (MAI) and lead iodide (PbI_2) in anhydrous DMF at 70 °C for 12 h. 80 μL of this freshly prepared $MAPbI_3$ perovskite solution (45 wt%) was spin-coated on the mp-TiO_2/blocking layer TiO_2/FTO substrate at 5000 rpm for 30 s. After a 4 s delay time of the spin coating process, a 240 μL of anhydrous chlorobenzene was quickly dropped at the substrate. The substrate was kept for 60 min and then dried at 100 °C for 10 min. The colour of the annealed film changed from transparent to dark brown indicating the crystallization of the $MAPbI_3$ layer. Pre-prepared HTM solution with additives as mentioned in Supporting information was spin coated at 2200 rpm for 30 s. Finally, an 80 nm thick silver counter electrode was deposited under high vacuum by thermal evaporation. The active area of this

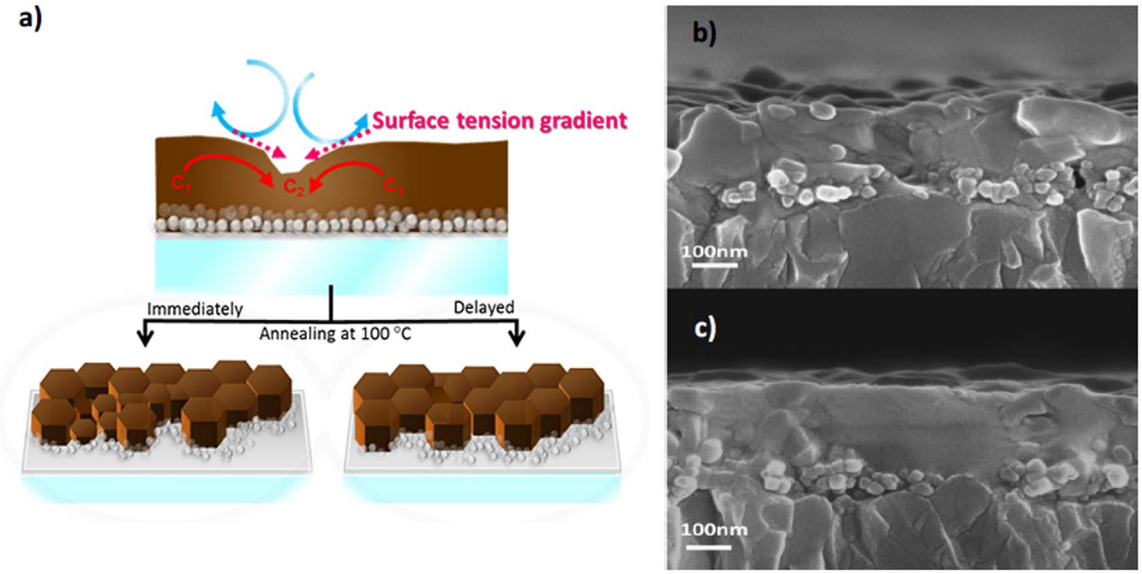

Fig. 3. a) Schematic demonstration showing the morphological improvement for the perovskite film with a delayed annealing treatment; b) SEM side-view image without delayed annealing; c) SEM side-view image with delayed annealing for 1 h.

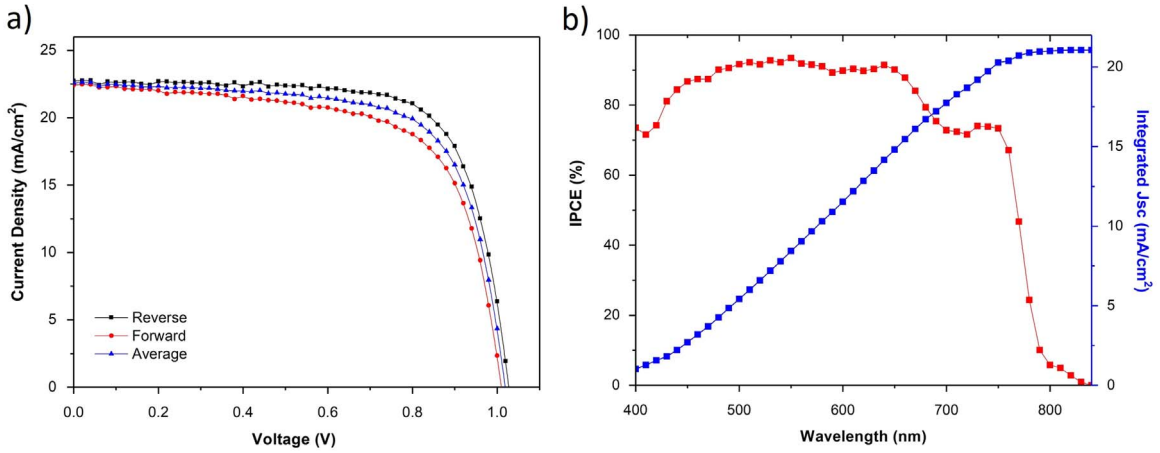

Fig. 4. a) *J-V* curves for the best cell measured by forward and reverse scans; b) IPCE spectra for the best cell.

Table 1
Photovoltaic parameters of the champion device.

	Jsc [mA cm^{-2}]	*Voc* [V]	*FF*	η [%]
Reverse	22.7	1.02	0.73	16.9
Forward	22.4	1.01	0.66	15.0
Average	22.6	1.01	0.69	16.0

electrode was fixed at 0.09 cm^2 using a metal mask.

2.2. Morphological characterization

The cross-section morphology of PSCs was investigated using dual beam focused ion beam system (DFIB), FEI Nova 600, combined SEM instrument. Prior to performing the cross-section milling, a 200 nm thick Pt protecting layer was deposited on the sample surface. Milling of the cross section was achieved with a gallium ion source at 52° tilting angle. The surface morphology was checked with Field-Emission Scanning Electron Microscope (FE-SEM) Zeiss Ultra Plus and Asylum Research MFP-3D AFM. The elemental analysis was also performed

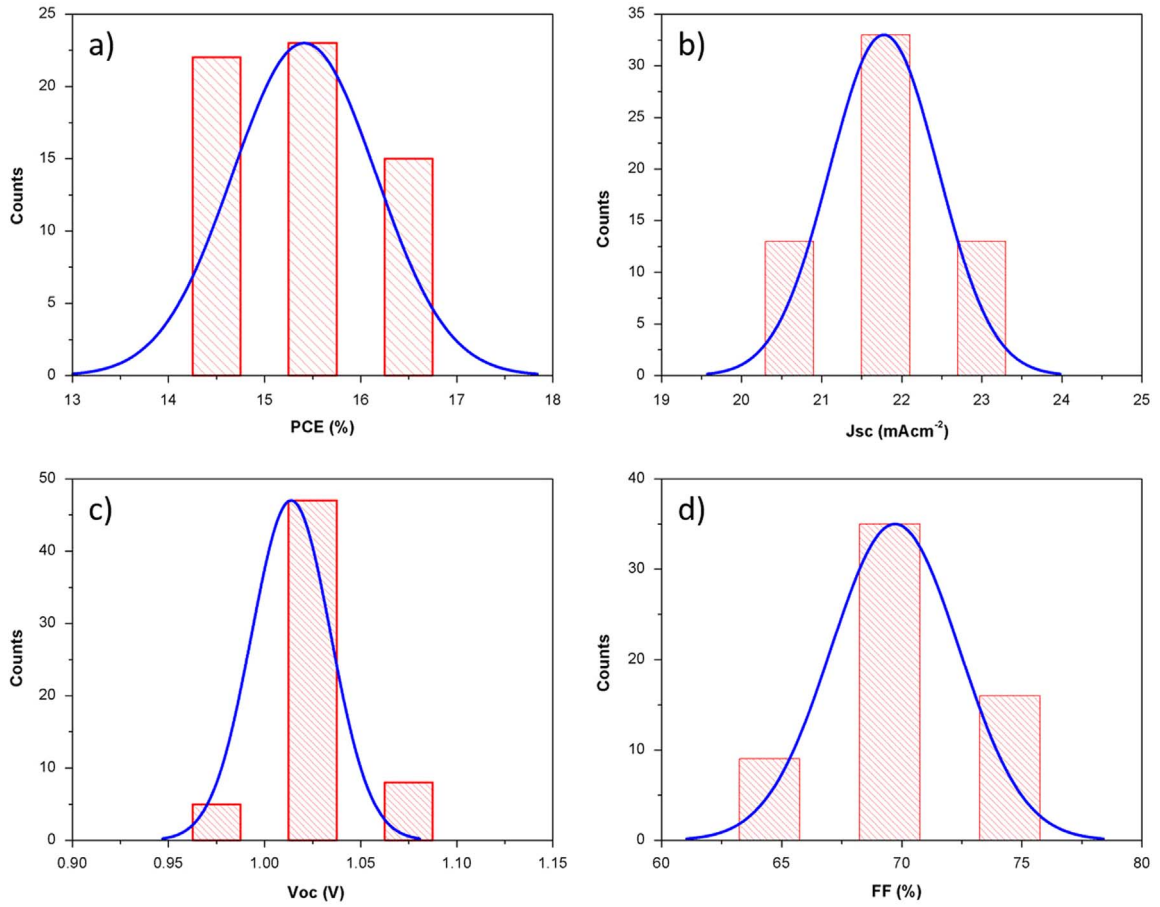

Fig. 5. Histogram for 60 devices; a) PCE, b) Jsc, c) Voc, d) FF.

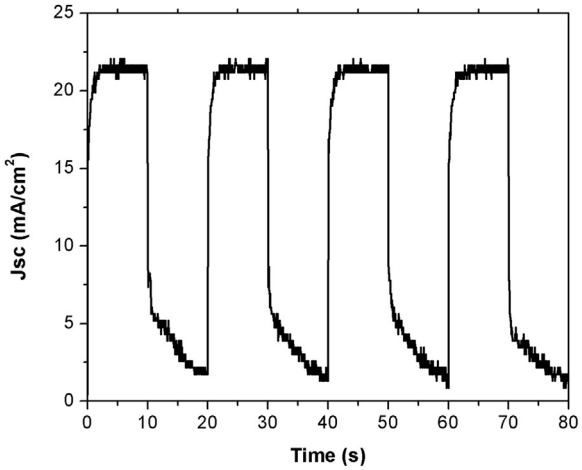

Fig. 6. Photocurrent behaviour of PSCs under ON-OFF cycles of illumination.

using energy dispersive X-ray (EDX) spectroscopy (Oxford X-Max) combined with FE-SEM on the device cross section. The elemental mapping is carried out to qualitatively study the distribution of the deposited layers on the substrate.

2.3. Photovoltaic characterization

The *J-V* curves were measured using a solar simulator (Newport, Oriel Instruments, 91160A) with a source meter (Keithley 2400) AM 1.5 G illumination at 100 mW/cm^2. A Si-reference cell (Newport, Oriel Instruments, 91150) certified by NREL was used to calibrate the output of the light source of the solar simulator. The incident photon-to-current conversion efficiency (IPCE) was measured using a power source (Newport, 300 W xenon lamp) with a monochromator (Newport, Cornerstone 260) and a multimeter (Keithley 2401). The time-photocurrent profile during ON-OFF illumination was recorded using a digital oscilloscope (GW Instek, GDS-1152A, 150 MHz).

3. Results and discussion

3.1. Solvent-assisted crystallization (SAC)

Schematic cartoon illustration of the SAC method is depicted in Fig. 1a. Using this chlorobenzene initiated SAC method with delayed annealing for 60 min the champion cell attained PCE 16.9% with the average efficiency 15.4% (s.d. ± 0.74) for sixty devices prepared under the same experimental conditions.

The addition of chlorobenzene on the spinning substrates at different times after the start of spin-coating (2 s, 4 s, and without adding any chlorobenzene) were conducted to optimize the condition of solvent assisted crystallization (SAC) method. Atomic force microscopy (AFM) and scanning electron microscopy (SEM) analysis were performed to get an insight of the surface morphologies of these films. Very distinct surface morphologies of the $MAPbI_3$ perovskite films were observed. As displayed in Fig. 1b, the addition of chlorobenzene after 4 s resulted in the uniform layer formed over an entire substrate with large grain size. For comparison, we also prepared films without SAC and with the addition of chlorobenzene at varied delay times. When the films were prepared without SAC, rod-like grains were formed with an incomplete surface coverage. With a delay time of 2 s, large voids between crystal boundaries were observed indicating defects in the surface, while the delay time of 6 s resulted in again the formation of rod-like grains with low surface coverage. These observations are in good accordance with the previous report on planar heterojunction architecture [35].

3.2. Delayed annealing effect

The effect of delayed annealing on photovoltaic performances of the devices was evaluated under standard AM 1.5 G illumination at the one-sun intensity (100 mW cm^{-2}). Fig. 2 shows the photovoltaic performance of the SAC-treated devices as a function of annealing delayed period. The PCEs of the devices exhibited great variations without an annealing delay, and the maximum efficiency with high current density and fill factor can be obtained when the devices were annealed at a delay time 60 min. We explained this phenomenon being due to so-called “Marangoni effect“, for which the rough perovskite surface resulted from the mass transfer of two solvents (DMF and chlorobenzene) with a gradient in surface tension. The idea to decrease the effect of Marangoni fluid in film formation was to make crystallization of perovskite with slow drying. In our approach, a second non-polar solvent (chlorobenzene) was injected into the wet perovskite film with the polar DMF solvent to reach the super-saturation condition. The sudden turbulence from the second solvent injection greatly causes liquid-solid phase separations and inhomogeneous concentrations so as to form tension gradient differences on the surface of perovskite before evaporation of the solvents. The delayed annealing had the effect to balance the surface tension gradient of the Marangoni fluid for surface smoothing and morphology ameliorating as reported for polymer solar cells [42–45].

As demonstrated in Fig. 3a, when the anti-solvent treated wet-perovskite film was annealed at 100 °C without a delay, the surface tension gradient would cause random crystallization of perovskite to give a rough surface. This can be seen from the SEM image (Fig. 3b) showing the roughness on perovskite surface. In contrast, the SEM image of Fig. 3c shows a much smoother surface with delay annealing for 1 h. Therefore, random crystallization on the perovskite surface can be avoided when a delay is applied before annealing. Moreover, the delayed annealing may also slow down the crystal growth before nucleation is completed. Therefore, uniform and flat perovskite film can be produced using this SAC approach followed by a delayed annealing.

3.3. Photovoltaic performance of champion cell

The current-voltage curves of the champion device are shown in Fig. 4a, for which the best performance was obtained when the *J-V* scan

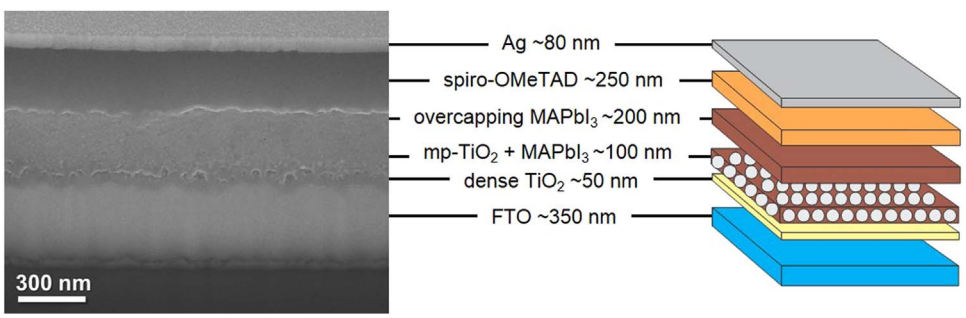

Fig. 7. Cross-sectional SEM image of the best-performing device prepared by FIB milling.

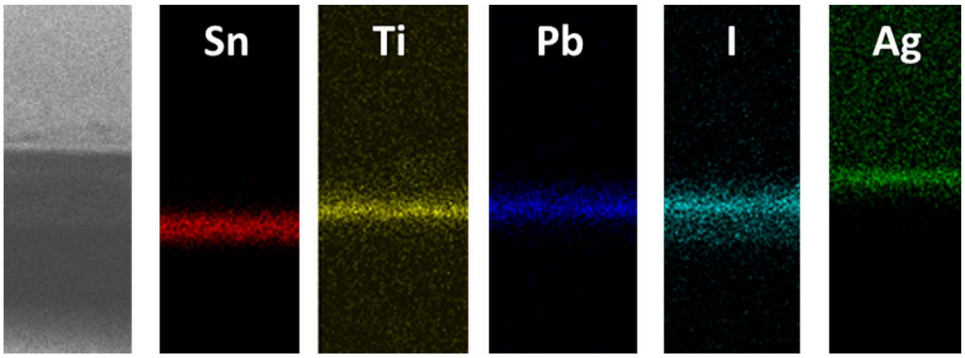

Fig. 8. Elemental EDX mapping of the mesoscopic perovskite solar cell.

was made in the reverse direction (from the open-circuit voltage (*Voc*) to the short-circuit current density (*Jsc*)), giving the values *Jsc* of 22.7 mA cm^{-2}, *Voc* of 1.02 V, fill factor (*FF*) of 0.73 and the PCE of 16.9%. The *Jsc*, *Voc* and *FF* values obtained from the *J-V* curve of the forward scan (from *Jsc* to *Voc*) were 22.4 mA cm^{-2}, 1.01 V and 0.66, respectively, yielding a PCE of 15.0%. The average *Jsc*, *Voc*, *FF,* and PCE of the best device measured under different scan direction were 22.6 mA cm^{-2}, 1.01 V, 0.69, and 16.0%. Photovoltaic data of 60 individual PSC devices are depicted in Table S1, supporting information (SI). The photovoltaic parameters of our champion device are summarized in Table 1. We also tested the performance of the planar device under similar experimental conditions for comparison. The best planar device featured with *Jsc* of 20.5 mA cm^{-2}, *Voc* of 1.00 V, *FF* of 0.65 and PCE of 13.3% under reverse scan direction, while under forward scan direction the device exhibited *Jsc* of 16.65 mA cm^{-2}, *Voc* of 1.02 V, *FF* of 0.53 and PCE of 9.0%. The larger hysteresis for the planar devices compared to the hybrid mesoscopic device is in good agreement with the previous reports [16,23,26,27].

The trends in the *J-V* curves can be well understood from the incident photon-to-current conversion efficiency (IPCE) spectra. The best device displayed a very broad IPCE plateau of over 80% covering the whole visible region as displayed in Fig. 4b. Integration of the IPCE spectrum over the AM 1.5 G solar photon flux yields a photocurrent density of 21.06 mA cm^{-2}, which is in reasonable agreement with the value obtained from the *J-V* scan (Table 1). The difference in the *Jsc* values obtained from measurement and the integration of the IPCE spectrum might be due to the different light intensity, mismatch in the absorption spectrum and testing mask aperture effect.

To check the reproducibility of the current approach we prepared 60 devices in different batches and measured their photovoltaic performance. The histograms of these 60 devices are displayed in Fig. 5. In general, the devices exhibit Voc from 0.96 to 1.06 V (s.d. ± 0.02), Jsc from 20.24 to 23.38 mA/cm^2 (s.d. ± 0.68), FF from 63.12% to 74.16% (s.d. ± 2.67), and resulting PCE from 14.22% to 16.92% (s.d. ± 0.75). The PCEs distribution plot for 60 devices tested under simulated AM 1.5 G at one sun illumination (100 mW/cm^2) presented in Fig. 5a shows that most of the devices result PCEs in the range of 15–16%. The average efficiency calculated for all sixty devices was 15.4%, proving the consistency, stability, and reproducibility of our method. Moreover, the average efficiency of 16.4% (s.d. ± 0.27) is calculated for top 15 devices with efficiencies higher than 16% (Table S2, SI). The excellent reproducibility is an important factor for large-scale production of these PSCs.

The consistency and stability of the devices in this study could be well understood from the ON-OFF properties depicted in Fig. 6. The photocurrent response was measured under illumination at ON-OFF interval of 10 s for 4 cycles. It is worth mentioning that the photocurrent of the PSCs device are all reproducible and consistent with quick response through multiple cycles, showing the stability of the device.

3.4. Cross-sectional SEM and EDX-SEM

The uniform nature and the thickness of the individual layers can be visualized from the cross-sectional SEM image (Fig. 7). This cross-sectional image was prepared for the best performing device using focused ion beam (FIB) milling. As shown from the figure, the device is composed of a c-TiO_2 layer (50 nm), a mp-TiO_2 layer (100 nm) with well-infiltrated $MAPbI_3$, a uniform $MAPbI_3$ capping layer (200 nm), a spiro-OMeTAD HTM layer (250 nm) and a silver counter electrode (80 nm). The mp-TiO_2 layer cannot be seen clearly in Fig. 6 as the sample is sputter-etched through the layer resulting very smooth cross-section morphology during the FIB milling. The clear mp-TiO_2 layer can be seen from the SEM image of the device prepared without FIB milling (SI, Fig. S1).

The elemental mapping is carried out by EDX-SEM to qualitatively study the distribution of the deposited layers on the substrate (Fig. 8). Based on the elemental analysis, five elements tin (Sn), titanium (Ti), lead (Pb), iodide (I) and silver (Ag) respectively, were found in the device. These elements were in qualitative agreement with the materials deposited on the substrate.

4. Conclusions

We report the fabrication of uniform and smooth perovskite films using solvent-assisted crystallization (SAC) followed by a delayed annealing to obtain the performance of the best device attaining PCE 16.9% under standard one-sun condition (AM 1.5 G illumination, 100 mW/cm^2). Moreover, the average efficiency 15.4% obtained from over sixty devices from different batches indicates the stability and consistency of the PSC devices prepared using this method. A delay time before annealing would prevent random crystallization on the perovskite surface. The delayed annealing resulted in smoother perovskite layer surface because the crystal growth slowed down before nucleation was completed. The use of easily available and cheaper ingredients to assemble the efficient PSC devices makes this method ample cost-effective for large-scale production. We believe that this procedure will lead toward the simple, economical and very much reproducible fabrication of highly efficient perovskite solar cells.

Acknowledgements

We thank Dr. C.-T. Chen and Dr. J.-T. Lin for the assistance with instrumentation. We also greatly acknowledge the SEM facility in Institute of Physics, Academia Sinica for the help to prepare the FIB sample. The authors also thank Ministry of Science and Technology (MOST) 103-2119-M-009-005 for financial assistance.

Appendix A. Supplementary material

Supplementary data associated with this article can be found in the online version at http://dx.doi.org/10.1016/j.solmat.2017.07.043.

References

[1] A. Yella, H.-W. Lee, H.N. Tsao, C. Yi, A.K. Chandiran, M.K. Nazeeruddin, E.W.-G. Diau, C.-Y. Yeh, S.M. Zakeeruddin, M. Grätzel, porphyrin-sensitized solar cells with cobalt (II/III)–based redox electrolyte exceed 12 percent efficiency, Science 334 (2011) 629–634.

[2] J.H. Rhee, C.-C. Chung, E.W.-G. Diau, A perspective of mesoscopic solar cells based on metal chalcogenide quantum dots and organometal-halide perovskites, NPG Asia Mater. 5 (2013) e68.

[3] I.J. Kramer, E.H. Sargent, The architecture of colloidal quantum dot solar cells: materials to devices, Chem. Rev. 114 (2014) 863–882.

[4] G. Li, R. Zhu, Y. Yang, Polymer solar cells, Nat. Photonics 6 (2012) 153–161.

[5] D.N. Congreve, J. Lee, N.J. Thompson, E. Hontz, S.R. Yost, P.D. Reusswig, M.E. Bahlke, S. Reineke, T. Van Voorhis, M.A. Baldo, External quantum efficiency above 100% in a singlet-exciton-fission–based organic photovoltaic cell, Science 340 (2013) 334–337.

[6] J.A. Chang, J.H. Rhee, S.H. Im, Y.H. Lee, H.-J. Kim, S.I. Seok, M.K. Nazeeruddin, M. Gratzel, High-performance nanostructured inorganic – organic heterojunction solar cells, Nano Lett. 10 (2010) 2609–2612.

[7] J.H. Noh, S.H. Im, J.H. Heo, T.N. Mandal, S.I. Seok, Chemical management for colorful, efficient, and stable inorganic–organic hybrid nanostructured solar cells, Nano Lett. 13 (2013) 1764–1769.

[8] J.H. Heo, S.H. Im, J.H. Noh, T.N. Mandal, C.-S. Lim, J.A. Chang, Y.H. Lee, H.-j. Kim, A. Sarkar, K. NazeeruddinMd, M. Gratzel, S.I. Seok, Efficient inorganic-organic hybrid heterojunction solar cells containing perovskite compound and polymeric hole conductors, Nat. Photonics 7 (2013) 486–491.

[9] S.D. Stranks, G.E. Eperon, G. Grancini, C. Menelaou, M.J.P. Alcocer, T. Leijtens, L.M. Herz, A. Petrozza, H.J. Snaith, Electron-hole diffusion lengths exceeding 1 μm in an organometal trihalide perovskite absorber, Science 342 (2013) 341–344.

[10] G. Xing, N. Mathews, S. Sun, S.S. Lim, Y.M. Lam, M. Grätzel, S. Mhaisalkar, T.C. Sum, Long-range balanced electron- and hole-transport lengths in organic-inorganic CH3NH3PbI3, Science 342 (2013) 344–347.

[11] A. Kojima, K. Teshima, Y. Shirai, T. Miyasaka, Organometal halide perovskites as visible-light sensitizers for photovoltaic cells, J. Am. Chem. Soc. 131 (2009) 6050–6051.

[12] W.S. Yang, J.H. Noh, N.J. Jeon, Y.C. Kim, S. Ryu, J. Seo, S.I. Seok, High-performance photovoltaic perovskite layers fabricated through intramolecular exchange, Science 348 (2015) 1234–1237.

[13] NREL, Best Research-Cell Efficiencies, in, 2017.

[14] J.-H. Im, I.-H. Jang, N. Pellet, M. Grätzel, N.-G. Park, Growth of CH3NH3PbI3 cuboids with controlled size for high-efficiency perovskite solar cells, Nat. Nano 9 (2014) 927–932.

[15] N.J. Jeon, H.G. Lee, Y.C. Kim, J. Seo, J.H. Noh, J. Lee, S.I. Seok, o-Methoxy substituents in Spiro-OMeTAD for efficient inorganic–organic hybrid perovskite solar cells, J. Am. Chem. Soc. 136 (2014) 7837–7840.

[16] N.J. Jeon, J.H. Noh, Y.C. Kim, W.S. Yang, S. Ryu, S.I. Seok, Solvent engineering for high-performance inorganic–organic hybrid perovskite solar cells, Nat. Mater. 13 (2014) 897–903.

[17] J.-W. Lee, D.-J. Seol, A.-N. Cho, N.-G. Park, High-efficiency perovskite solar cells based on the black polymorph of HC(NH2)2PbI3, Adv. Mater. 26 (2014) 4991–4998.

[18] S. Ryu, J.H. Noh, N.J. Jeon, Y. Chan Kim, W.S. Yang, J. Seo, S.I. Seok, Voltage output of efficient perovskite solar cells with high open-circuit voltage and fill factor, Energy Environ. Sci. 7 (2014) 2614–2618.

[19] N.J. Jeon, J.H. Noh, W.S. Yang, Y.C. Kim, S. Ryu, J. Seo, S.I. Seok, Compositional engineering of perovskite materials for high-performance solar cells, Nature 517 (2015) 476–480.

[20] H. Zhou, Q. Chen, G. Li, S. Luo, T.-B. Song, H.-S. Duan, Z. Hong, J. You, Y. Liu, Y. Yang, Interface engineering of highly efficient perovskite solar cells, Science 345 (2014) 542–546.

[21] W. Nie, H. Tsai, R. Asadpour, J.-C. Blancon, A.J. Neukirch, G. Gupta, J.J. Crochet, M. Chhowalla, S. Tretiak, M.A. Alam, H.-L. Wang, A.D. Mohite, High-efficiency solution-processed perovskite solar cells with millimeter-scale grains, Science 347 (2015) 522–525.

[22] M. Gratzel, The light and shade of perovskite solar cells, Nat. Mater. 13 (2014) 838–842.

[23] H.-S. Kim, N.-G. Park, Parameters affecting I–V hysteresis of CH3NH3PbI3 perovskite solar cells: effects of perovskite crystal size and mesoporous TiO2 layer, J. Phys. Chem. Lett. 5 (2014) 2927–2934.

[24] M.D. McGehee, Perovskite solar cells: continuing to soar, Nat. Mater. 13 (2014) 845–846.

[25] R.S. Sanchez, V. Gonzalez-Pedro, J.-W. Lee, N.-G. Park, Y.S. Kang, I. Mora-Sero, J. Bisquert, Slow dynamic processes in lead halide perovskite solar cells. Characteristic times and hysteresis, J. Phys. Chem. Lett. 5 (2014) 2357–2363.

[26] H.J. Snaith, A. Abate, J.M. Ball, G.E. Eperon, T. Leijtens, N.K. Noel, S.D. Stranks, J.T.-W. Wang, K. Wojciechowski, W. Zhang, Anomalous hysteresis in perovskite solar cells, J. Phys. Chem. Lett. 5 (2014) 1511–1515.

[27] E.L. Unger, E.T. Hoke, C.D. Bailie, W.H. Nguyen, A.R. Bowring, T. Heumuller, M.G. Christoforo, M.D. McGehee, Hysteresis and transient behavior in current-voltage measurements of hybrid-perovskite absorber solar cells, Energy Environ. Sci. 7 (2014) 3690–3698.

[28] Z. Hameiri, A. Mahboubi Soufiani, M.K. Juhl, L. Jiang, F. Huang, Y.-B. Cheng, H. Kampwerth, J.W. Weber, M.A. Green, T. Trupke, Photoluminescence and electroluminescence imaging of perovskite solar cells, Prog. Photovolt.: Res. Appl. 23 (2015) 1697–1705.

[29] S. Mastroianni, F.D. Heinz, J.H. Im, W. Veurman, M. Padilla, M.C. Schubert, U. Wurfel, M. Gratzel, N.G. Park, A. Hinsch, Analysing the effect of crystal size and structure in highly efficient CH3NH3PbI3 perovskite solar cells by spatially resolved photo- and electroluminescence imaging, Nanoscale 7 (2015) 19653–19662.

[30] D.W. de Quilettes, S.M. Vorpahl, S.D. Stranks, H. Nagaoka, G.E. Eperon, M.E. Ziffer, H.J. Snaith, D.S. Ginger, Impact of microstructure on local carrier lifetime in perovskite solar cells, Science 348 (2015) 683–686.

[31] H.-S. Kim, C.-R. Lee, J.-H. Im, K.-B. Lee, T. Moehl, A. Marchioro, S.-J. Moon, R. Humphry-Baker, J.-H. Yum, J.E. Moser, M. Gratzel, N.-G. Park, Lead iodide perovskite sensitized all-solid-state submicron thin film mesoscopic solar cell with efficiency exceeding 9%, Sci. Rep. 2 (2012) 591.

[32] M.M. Lee, J. Teuscher, T. Miyasaka, T.N. Murakami, H.J. Snaith, Efficient hybrid solar cells based on meso-superstructured organometal halide perovskites, Science 338 (2012) 643–647.

[33] J. Burschka, N. Pellet, S.-J. Moon, R. Humphry-Baker, P. Gao, M.K. Nazeeruddin, M. Gratzel, Sequential deposition as a route to high-performance perovskite-sensitized solar cells, Nature 499 (2013) 316–319.

[34] M. Liu, M.B. Johnston, H.J. Snaith, Efficient planar heterojunction perovskite solar cells by vapour deposition, Nature 501 (2013) 395–398.

[35] M. Xiao, F. Huang, W. Huang, Y. Dkhissi, Y. Zhu, J. Etheridge, A. Gray-Weale, U. Bach, Y.-B. Cheng, L. Spiccia, A Fast Deposition-Crystallization, Procedure for highly efficient lead iodide perovskite thin-film solar cells, Angew. Chem. 126 (2014) 10056–10061.

[36] Z. Xiao, Q. Dong, C. Bi, Y. Shao, Y. Yuan, J. Huang, Solvent annealing of perovskite-induced crystal growth for photovoltaic-device efficiency enhancement, Adv. Mater. 26 (2014) 6503–6509.

[37] J. Liu, C. Gao, X. He, Q. Ye, L. Ouyang, D. Zhuang, C. Liao, J. Mei, W. Lau, Improved crystallization of perovskite films by optimized solvent annealing for high efficiency solar cell, ACS Appl. Mater. Interfaces 7 (2015) 24008–24015.

[38] Z. Zhou, L. Huang, X. Mei, Y. Zhao, Z. Lin, H. Zhen, Q. Ling, Highly reproducible and photocurrent hysteresis-less planar perovskite solar cells with a modified solvent annealing method, Sol. Energy 136 (2016) 210–216.

[39] Y. Liu, I. Shin, I.-W. Hwang, J. Lee, S. Kim, D.Y. Lee, S.-H. Lee, J.-W. Jang, Y.K. Jung, J.H. Jeong, S.H. Park, K.H. Kim, Effective hot-air annealing for improving the performance of perovskite solar cells, Sol. Energy 146 (2017) 359–367.

[40] J. Ye, L. Zhu, L. Zhou, X. Liu, X. Zhang, H. Zheng, G. Liu, Z. Shao, X. Pan, S. Dai, Effective and reproducible method for preparing low defects perovskite film toward highly photoelectric properties with large fill factor by shaping capping layer, Sol. Energy 136 (2016) 505–514.

[41] N. Ahn, D.-Y. Son, I.-H. Jang, S.M. Kang, M. Choi, N.-G. Park, Highly reproducible perovskite solar cells with average efficiency of 18.3% and best efficiency of 19.7% fabricated via lewis base adduct of lead(II) iodide, J. Am. Chem. Soc. 137 (2015) 8696–8699.

[42] S. Kojima, T. Moriga, K. Takenouchi, The leveling of thermosetting waterborne coatings. Part I: observation of leveling process, Polym. Eng. Sci. 33 (1993) 1320–1328.

[43] S. Kojima, T. Moriga, K. Takenouchi, The leveling of thermosetting waterborne coatings. Part III: leveling under controlled conditions, Polym. Eng. Sci. 35 (1995) 1949–1954.

[44] C. Girotto, D. Moia, B.P. Rand, P. Heremans, High-performance organic solar cells with spray-coated hole-transport and active layers, Adv. Funct. Mater. 21 (2011) 64–72.

[45] C. Hsin-Yi, S. Lan, P.-C. Yang, S.-H. Lin, J.-Y. Sun, C.-F. Lin, Poly(3-hexylthiophene): indene-C60 bisadduct morphology improvement by the use of polyvinylcarbazole as additive, Sol. Energy Mater. Sol. Cells 113 (2013) 90–95.